Available online at www.sciencedirect.com
ScienceDirect
Trans. Nonferrous Met. Soc. China 33(2023) 1988−2000
Transactions of Nonferrous Metals Society of China
www.tnmsc.cn

Enhanced mechanical properties of aluminum matrix composites reinforced with high-entropy alloy particles via asymmetric cryorolling

Kai-guang LUO[1,2], Yu-ze WU[1,2], Han-qing XIONG[1,2], Yun ZHANG[1,2], Charlie KONG[3], Hai-liang YU[1,2,4]

1. State Key Laboratory of Precision Manufacturing for Extreme Service Performance, Central South University, Changsha 410083, China;
2. School of Mechanical and Electrical Engineering, Central South University, Changsha 410083, China;
3. Mark Wainwright Analytical Centre, University of New South Wales, Sydney, NSW 2052, Australia;
4. Light Alloys Research Institute, Central South University, Changsha 410083, China

Received 27 January 2022; accepted 27 May 2022

Abstract: To achieve higher performance of aluminum matrix composites (AMCs), high-entropy alloy particles (HEA_p)-reinforced AMCs sheets were processed via asymmetric rolling (AR, 298 K) and asymmetric cryorolling (ACR, 77 K) methods. The mechanical properties and microstructure of the HEA_p/AMCs were analyzed by tensile tests, scanning electron microscopy (SEM), and transmission electron microscopy (TEM). The results suggest that ACR improved the mechanical properties of HEA_p/AMCs to a higher degree than AR. The ultimate tensile strength (UTS) of ACR 3 wt.% HEA_p/AMCs reached 253 MPa, which was 13.5% higher than that achieved with AR. ACR resulted in fewer microvoids, finer grain sizes, and higher dislocation density in HEA_p/AMC sheets compared to AR. Such a reduction of defects during ACR can be attributed to the volume shrinkage effect of the HEA_p/AMCs in the cryogenic environment.

Key words: aluminum matrix composites; $Al_{0.5}CoCrFeNi$ high-entropy alloy particles; asymmetric cryorolling; grain size; micro defects

1 Introduction

Particle-reinforced aluminum matrix composites (PAMCs) [1,2] are the most famous metal matrix composites which have wide applications in aerospace [3] and automotive industries [4]. This specifically arises from their high specific strength [5], excellent stiffness [6], and good wear resistance [7]. Ceramic particles with high strength and elastic moduli, such as SiC and TiC particles, are often used in AMCs nowadays [8]. However, the ductility of such AMCs decreases significantly owing to the poor deformation ability of ceramic particles. Additionally, the secondary processing of such AMCs is challenging due to the discordant deformation of ceramic particles and the aluminum matrix [5]. Therefore, it is of real importance to seek new kinds of reinforcing particles and processing technology to develop PAMC sheets.

High-entropy alloys (HEAs) have high strength, good plasticity, and excellent cryogenic-temperature mechanical properties [9], which make them excellent candidates to act as reinforced particles in AMCs in recent years. LI et al [10] prepared AMCs reinforced by $Al_{0.8}CoCrFeNi$ high-entropy alloy particles (HEAp) through friction stir processing and found that the average hardness was remarkably enhanced from HV 80.5

Corresponding author: Hai-liang YU, E-mail: yuhailiang1980@tom.com, yuhailiang@csu.edu.cn;
Yun ZHANG, E-mail: yun_zhang66@163.com
DOI: 10.1016/S1003-6326(23)66238-7

(aluminum matrix) to HV 125.7 (AMCs). Attributed to the good bonding ability between the HEA particles (HEA_p) and aluminum matrix, the ultimate tensile strength (UTS) of the AMCs was 371 MPa. YUAN et al [11] fabricated AMCs reinforced with $Al_{0.6}CoCrFeNi$ HEA_p by a vacuum hot-pressing sintering process. After post annealing at 773 K for 12 h, the hardness of the AMCs could be enhanced from HV 136 to HV 178. A continuous interfacial layer was generated, which could transfer more loads from Al matrix to HEA_p. LIU et al [12] applied spark plasma sintering to prepare AlCoCrFeNi-reinforced AMCs and found that both the yield strength and ductility were enhanced with sintering temperature. LUO et al [13] compared the deformation behavior of HEA_p/ AMCs under room temperature rolling (RTR) and cryorolling. After cryorolling, the mechanical properties got better, and a low density of defects was observed compared to those obtained via RTR. LI et al [14] prepared HEA_p/AMCs by powder metallurgy. The nanohardness and elastic modulus at the interface was 1245 MPa and 72 GPa, respectively, which points toward an excellent interfacial bonding strength. However, for HEA_p/AMCs, defects such as microcracks were easily generated when deformed at room temperature. This, in turn, had a deteriorating effect on the bonding ability of the HEA_p and aluminum matrix [13]. In addition, the mismatch between the coefficient of thermal expansion of the HEA_p reinforcement and aluminum matrix may also accelerate the generation of micropores [15]. Therefore, it is necessary to develop new techniques that would strengthen HEA_p/AMCs.

Asymmetric rolling (AR) can reduce rolling force [16], improve sheet forming performance and mechanical properties [17]. Asymmetric cryorolling (ACR) is considered a severe plastic deformation process that benefits from the advantages of both AR and cryorolling [18]. The cryogenic environment in the ACR can effectively inhibit dynamic recovery, accumulate more dislocations, and promote grain refinement, resulting in higher tensile strength [19]. YU et al [20] prepared AA6061 sheets by ACR and observed that hardness and tensile strength were improved, and the grain size was refined to 235 nm after 7 ACR cycles. ZHANG et al [21] observed that the grains became finer, and the deformation twins appeared in CoCrNi sheets after ACR processing at 77 K, which resulted in excellent mechanical properties. However, there are only few studies on the development of HEA_p/AMCs by using ACR. The deformation behavior of HEA_p during shear deformation by ACR greatly affected the mechanical properties of AMCs. At present, the strengthening mechanism of HEA_p/AMCs by the ACR process was not clear. Therefore, it was very significant to explore the relationship between mechanical properties and microstructure of AMCs during ACR.

In the present study, the HEA_p/AMC sheets were processed by ACR (77 K) and AR (293 K), respectively. The mechanical properties and microstructure evolution of the HEA_p/AMC sheets after rolling were analyzed. Finally, the effect of plastic deformation in a cryogenic environment on the microstructure and mechanical properties of HEA_p/AMCs was discussed.

2 Experimental

In this study, commercial AA1050 (Al−0.25Si−0.4Fe−0.05Cu−0.05Mn−0.05Zn) ingot and $Al_{0.5}CoCrFeNi$ (Co−22.26Cr−23.17Fe−24.42Ni−5.81Al) HEA_p were selected as the matrix and the reinforcement of HEA_p/AMCs, respectively. HEA_p/AMC ingots were prepared by a stir casting process, as follows. A resistance furnace was used to melt AA1050 completely at 1093 K. After holding for 30 min for slag removal, HEA_p was wrapped in high purity aluminum foil and immersed in the molten liquid of aluminum alloy. After mechanical agitation, the composite solution was poured into the mold. Cuboid shape HEA_p/AMCs ingots were obtained. The aforementioned steps were repeated to obtain the HEA_p/AMCs ingots with mass fractions of 0, 1, and 3 wt.% HEA_p. The HEA_p/AMC ingots were cut into 2 mm-thick sheets before AR and ACR processing. The rolling temperatures employed in the AR and ACR were 298 and 77 K, respectively. Figure 1 illustrates a schematic diagram of the ACR processing. The HEA_p/AMC sheets were soaked in liquid nitrogen (77 K) for 5 min before each ACR cycle. The rolling speed ratio between the upper (V_1) and lower roll (V_2) was set to 1.4:1 for AR and ACR. The rolling reduction ratio of each pass was controlled between 10% and 20%. The rolling

temperature was the only variable factor that distinguished AR and ACR. After rolling, HEA_p/AMC sheets with rolling reduction ratios of 50% (1 mm), 80% (0.4 mm) and 95% (0.1 mm) were obtained.

The microhardness of the HEA_p/AMCs was measured using a Vickers microhardness tester (HXD−2000TMC/LCD 181101X) with a load of 0.5 N and a time duration of 15 s. The microhardness of each sample was randomly detected five times. Tensile samples were prepared utilizing an electrospark wire-electrode cutting machine along the rolling direction. The dimensions of the tensile samples are shown in Fig. 1(b). Tensile tests were carried out on a Shimadzu AGS−X 10 kN tensile machine at a strain rate of 1×10^{-3} s^{-1}. The tensile tests were repeated three times for each sample. A scanning electron microscope (SEM, TESCAN MIRA3 LMU) equipped with an energy dispersive spectrometer (EDS) was used to detect the morphology, microstructure, and element distribution of HEA_p. Furthermore, the microstructure of HEA_p/AMCs, specifically dislocations and grain size, was characterized by transmission electron microscopy (TEM, Philips CM200 field emission gun transmission electron microscope, 200 kV). TEM samples were prepared utilizing the focused ion beam technique.

3 Results

3.1 Microstructure of HEA_p/AMCs

The HEA_p and AMCs were characterized using SEM. Figure 2(a) shows the morphology of HEA_p. EDS was used to characterize the elements distribution in HEA_p. The distributions of Al, Fe, Co, Cr, and Ni elements in HEA_p were relatively uniform without any impurity element, as depicted in Figs. 2(b−f). The particle size distribution of HEA_p is shown in Fig. 2(g), and no obvious oversized particles were observed. The average particles size of HEA_p was 4.5 μm.

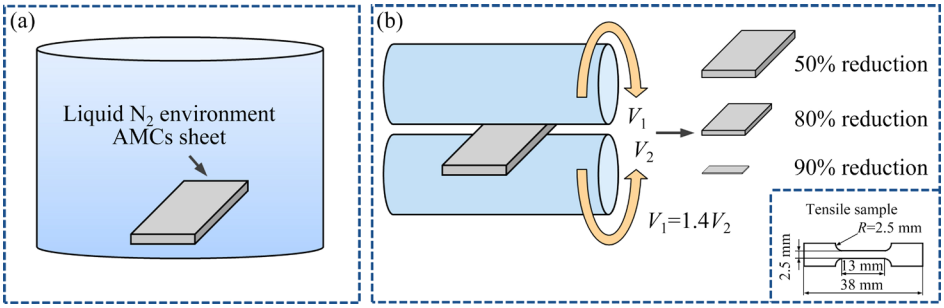

Fig. 1 Schematic diagram of asymmetric cryorolling: (a) Cryogenic treatment (77 K); (b) Asymmetric cryorolling

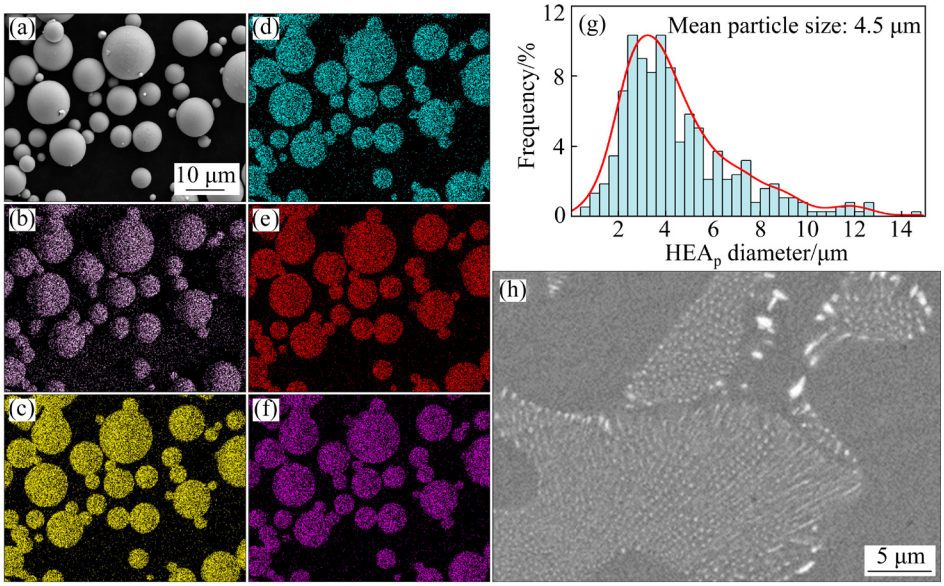

Fig. 2 SEM image of HEA_p (a); Element distributions of Al (b), Fe (c), Co (d), Cr (e), and Ni (f); HEA_p size distribution (g); SEM image of 3 wt.% HEA_p/AMCs before rolling (h)

The XRD results are shown in Fig. 3. Only the α(Al) phase existed in pure aluminum. A typical dual-phase structure of FCC+BCC was characterized for the HEA_p. In the 2θ range of 82°−83°, the peak intensity of pure aluminum was lower, while a relatively strong BCC phase peak from HEA_p was detected. In addition, the FCC phase corresponding to HEA_p was also detected in the 2θ range of 43°−44° from the 3 wt.% HEA_p/AMCs. However, due to a low mass fraction of HEA_p, the peak intensities were generally low. The XRD results were also utilized to quantitatively calculate the dislocation density of the composites by the Williamson Hall formula [18]:

$$\frac{\beta\cos\theta}{\lambda}=\frac{1}{D_v}+2e\left(\frac{2\sin\theta}{\lambda}\right) \quad (1)$$

$$\rho=\left(\rho_D\cdot\rho_s\right)^{1/2} \quad (2)$$

$$\rho_D=3/D_v^2 \quad (3)$$

$$\rho_s=K(e^2)/b^2 \quad (4)$$

where β is the integral breadth, θ is the diffraction angle, λ is the wavelength, D_v is the volume weighted crystallite size and e is the microstrain. ρ_D is the dislocation density due to the domain size, and ρ_s is the dislocation density due to strain broadening. K=6π, and b is the magnitude of Burgers vector for the FCC structure. Although the dislocation density measured by XRD was not precise, this method was reasonably good to evaluate the variation of dislocation density in HEA_p/AMCs during different rolling processes. The calculated results are listed in Table 1, and the data suggest that under the same rolling deformation, the dislocation densities of the AMCs obtained via the ACR process were higher than those obtained via AR.

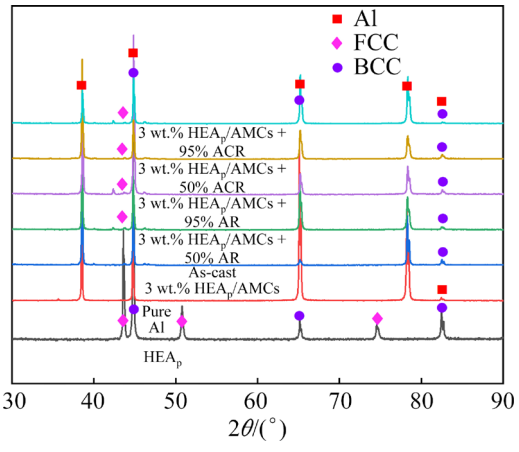

Fig. 3 XRD patterns of HEA_p and AMCs

Table 1 Calculation results of crystallite size and dislocation density of AMCs with different rolling processes

Process condition	Crystallite size/nm	Dislocation density/m^{-2}
95% AR	237	1.94×10^{14}
95% ACR	179	2.61×10^{14}

The microstructure of the 3 wt% HEAp/AMCs after 95% reduction via AR and ACR processes was characterized by the SEM. Figures 4(a, c) demonstrate the HEA_p reinforcement phase in the AMCs distributed along the rolling direction. The HEA_p size after ACR was significantly smaller than that after AR process, which could be intuitively observed from the higher magnification image in Figs. 4(b, d). Additionally, more microvoids and microcracks could be observed near the HEA_p reinforcement phase corresponding to AR HEA_p/AMCs. In contrast, none was found in ACR HEA_p/AMCs samples. The microvoids in Figs. 4(b, d) for AR and ACR processes were quantitatively evaluated. In the AR process, 39 micropores were identified in 588 μm^2 range, while only 11 micropores were observed in the corresponding ACR process. The number density of micropores in the AR process was 3.5 times that in the ACR process. In addition, the HEA_p reinforcement phase was smaller in the AMCs, and more nanoparticles appeared.

Figure 5 illustrates the TEM images of the 3 wt.% HEA_p/AMCs after AR and ACR with 95% reduction. Many dislocation lines appeared in the microstructure of the AR HEA_p/AMCs. Several microvoids were observed around the HEA_p during AR (Fig. 4(a)), which also appeared in the room temperature-rolled sheets [13]. Compared to the microstructure of AR HEA_p/AMCs, the grains of ACR HEA_p/AMCs were significantly refined. The grain structures <100 nm appeared locally in the ACR HEA_p/AMCs, while it was absent in the AR ones. Many tangled dislocation regions were generated in the ACR samples. Due to the high density of tangled dislocations, dislocation cell structures [22] were observed along with subgrain structures [23]. The HEA_p size of ACR HEA_p/AMCs was also remarkably smaller than that of AR ones, which was evident from the SEM result in

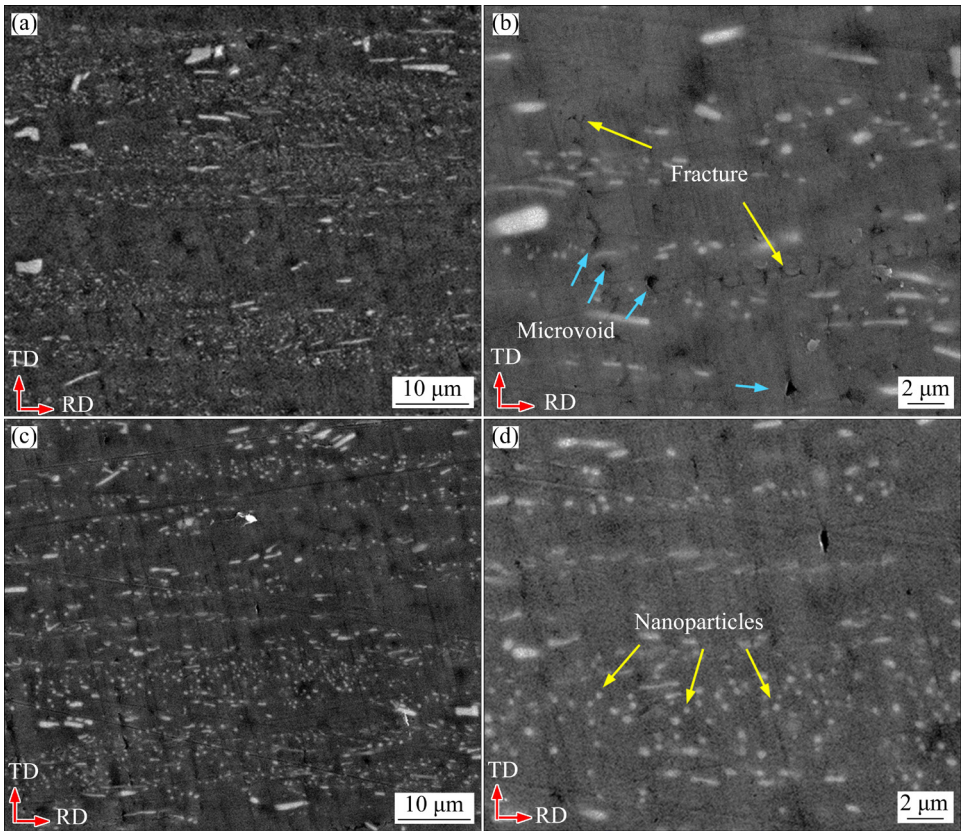

Fig. 4 SEM images of 3 wt.% HEA_p/AMCs after 95% rolling reduction by AR (a, b) and ACR (c, d) processes

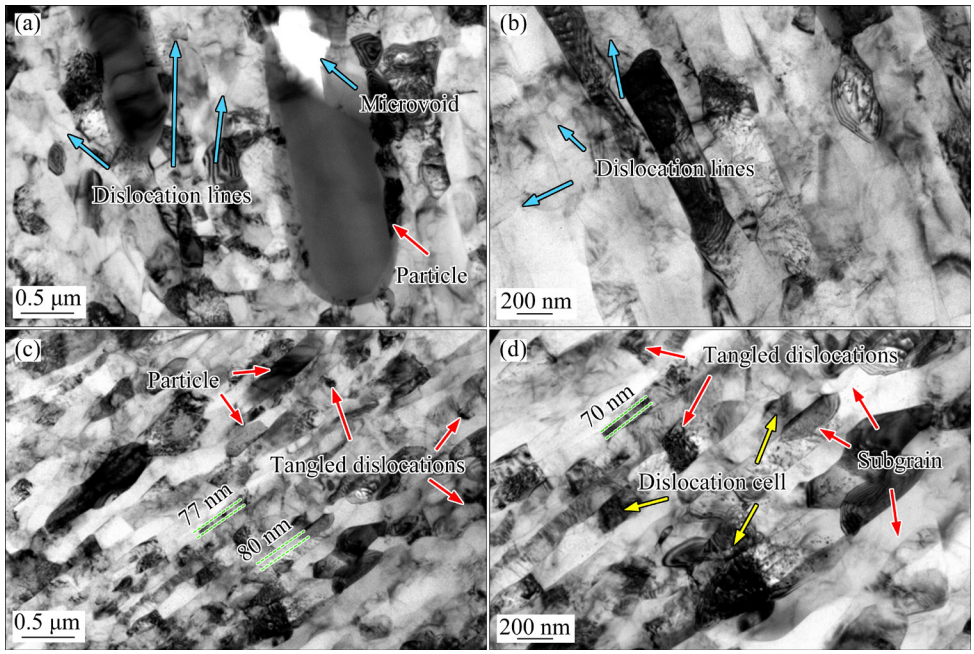

Fig. 5 TEM images of 3 wt.% HEA_p/AMCs with 95% rolling reduction via AR (a, b) and ACR (c, d) processes

Fig. 4. These special structures were significantly different from the AR HEA_p/AMCs, showing the unique advantages of the ACR process. No microvoids were detected in the ACR HEA_p/AMCs, which demonstrated a positive effect of the ACR process in avoiding defects in AMCs sheets [24].

The grain sizes of AR and ACR HEA_p/AMCs were statistically analyzed, as presented in Fig. 6. The average grain size of the AR HEA_p/AMCs was 237 nm (Fig. 6(a)), and that of ACR was 179 nm

(Fig. 6(b)). This result was also intuitively reflected in the TEM images in Fig. 5, which further affirmed that the grain size of 3 wt.% HEA_p/AMCs was refined by the ACR process.

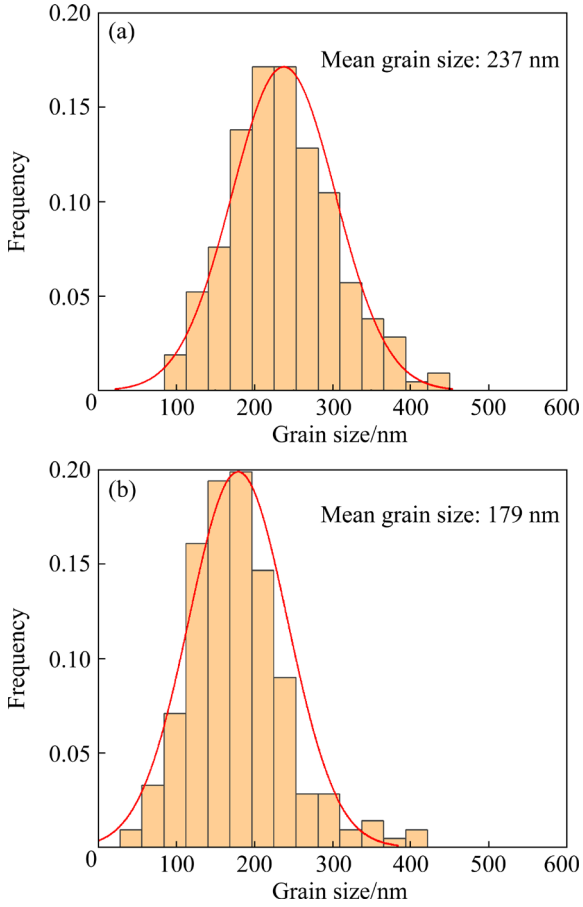

Fig. 6 Grain size distribution of 3 wt.% HEA_p/AMCs after 95% reduction via AR (a) and ACR (b)

3.2 Mechanical properties of HEA_p/AMCs

Figure 7 shows the microhardness values of HEA_p/AMCs with different rolling processes. With increasing rolling reduction, the microhardness value of HEA_p/AMCs gradually increased. The microhardness of ACR HEA_p/AMCs was higher than that of AR HEA_p/AMCs under the same rolling reduction. In Fig. 7(a), ACR showed a slight increase in the microhardness value of pure aluminum. With the increase in the mass fraction of HEA_p, ACR markedly improved the microhardness of the HEA_p/AMCs. When taking 3 wt.% HEA_p/AMCs as an example, under 50% rolling reduction, the microhardness of ACR HEA_p/AMCs was HV 74, and that of AR was HV 69. The microhardness of ACR HEA_p/AMCs was increased by 7.2% compared with that of AR HEA_p/AMCs. When the rolling reduction was increased from 80% to 90%, the microhardness value of the HEA_p/AMCs also increased from HV 76 to HV 84. These results suggest that the ACR process could significantly improve the microhardness of HEA_p/AMCs.

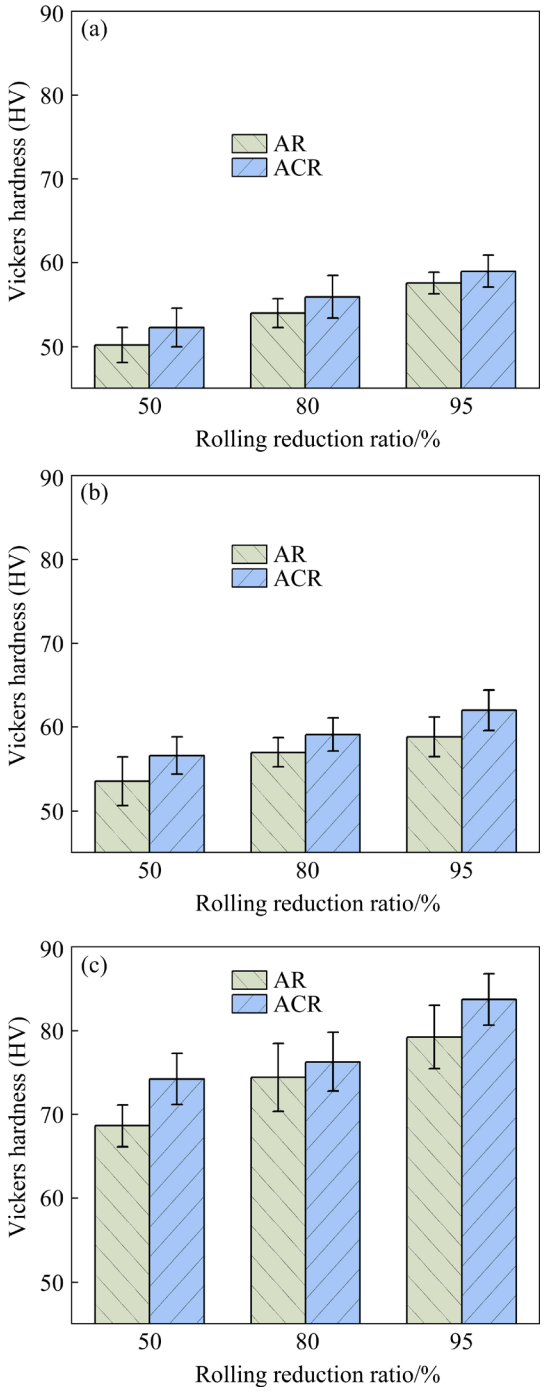

Fig. 7 Microhardness of HEA_p/AMCs: (a) 0 wt.% HEA_p; (b) 1 wt.% HEA_p; (c) 3 wt.% HEA_p

Figures 8 and 9 show the yield strength, ultimate tensile stress, and elongation values of the HEA_p/AMCs sheets after rolling. After rolling deformation, the mechanical properties of the ACR

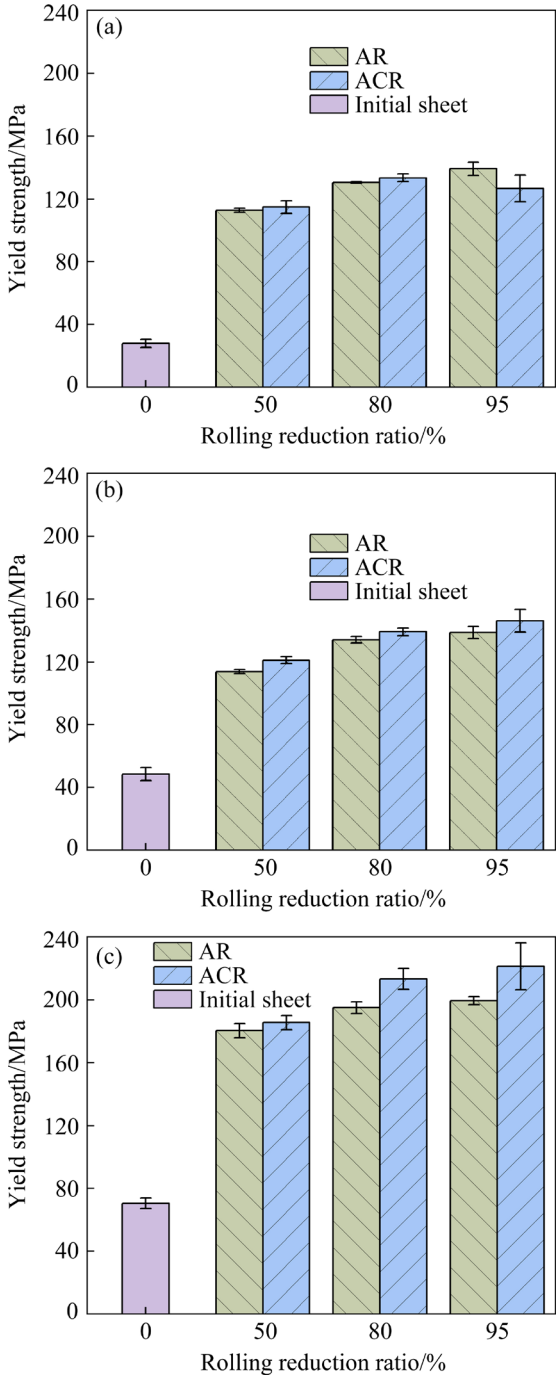

Fig. 8 Yield strength of HEA_p/AMC sheets via AR and ACR: (a) 0 wt.% HEA_p; (b) 1 wt.% HEA_p; (c) 3 wt.% HEA_p

HEA_p/AMCs got better than those of the AR HEA_p/AMCs. When considering 3 wt.% HEA_p/AMCs as an example, the yield strength of ACR samples was improved by 10.5% compared to AR. The yield strength was 195 MPa for AR samples, which increased to 213 MPa for ACR samples at a rolling reduction ratio of 80%. Similarly, the yield strength increased from 200 to 221 MPa when the

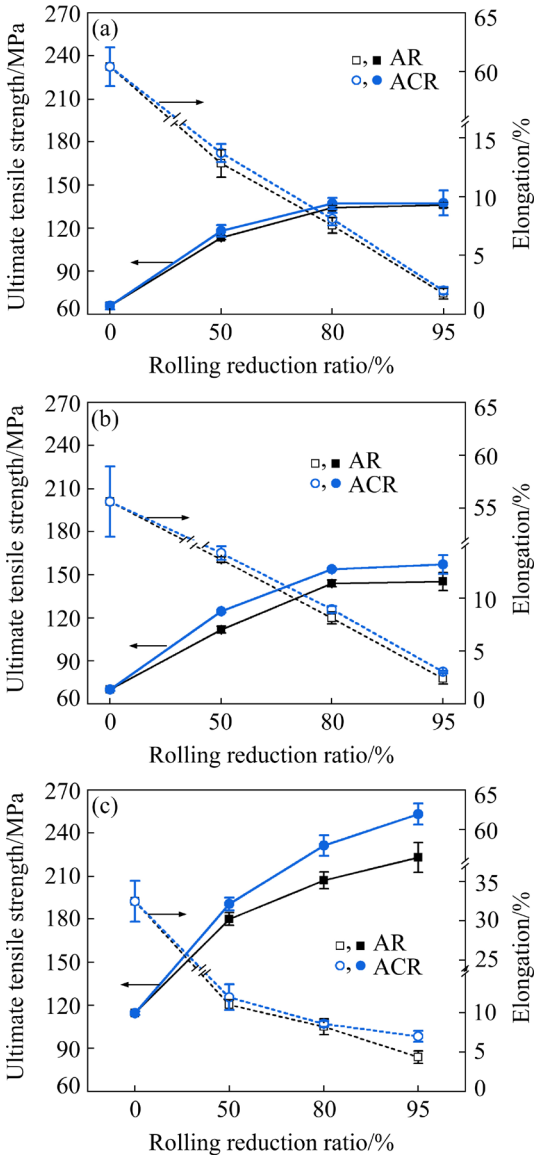

Fig. 9 Ultimate tensile strength and elongation of HEA_p/AMC sheets via AR and ACR: (a) 0 wt.% HEA_p; (b) 1 wt.% HEA_p; (c) 3 wt.% HEA_p

rolling reduction ratio was increased to 95%. The UTS of the ACR HEA_p/AMCs was 10.2% higher than that of the AR samples. The UTS of the initial HEA_p/AMCs was 115 MPa, which was markedly increased to 207 MPa for AR HEA_p/AMCs and 231 MPa for ACR HEA_p/AMCs at a rolling reduction ratio of 80%. After 95% rolling reduction, the UTS was 223 MPa for AR samples, while it reached 253 MPa for ACR sheets, approximately by 13.5% increase. Meanwhile, the elongation of the HEA_p/AMCs was 4.3% and 7%, respectively, for AR and ACR samples. Thus, it became obvious that both the strength and elongation were further enhanced by ACR.

3.3 Fracture morphology

Figures 10(a−c) show the tensile fracture morphologies of 3 wt.% HEA_p/AMC samples with different rolling reduction ratios after the AR and ACR processes. Under 50% rolling reduction, some dimples were generated on the tensile surface of AR HEA_p/AMCs (Fig. 10(a)). However, a larger number of dimples with enlarged dimensions could be observed in the ACR samples (Fig. 10(d)). Meanwhile, more evident tearing edges were observed in the AR HEAp/AMC tensile fracture morphology, unlike in the ACR samples [25]. Figures 10(b, e) show an interesting phenomenon. Large areas of cleavage surface appeared in the tensile fracture of AR HEA_p/AMCs [26], but the dimples were little in number and shallow. This reflected that the AR HEA_p/AMCs exhibited a brittle fracture mode at 80% rolling reduction. However, under the same deformation, the surface of tensile fracture in ACR HEA_p/AMCs showed great differences. A great density of dimples with a relatively large area were observed on the fracture surface. Every single dimple was deep, and only a few tearing edges appeared on the surface, suggesting a mixed-mode fracture characteristic [27]. Such a fracture morphology reflected that ACR HEA_p/AMCs still had a large elongation at 80% rolling reduction, which was in sharp contrast with AR samples. Under 95% rolling reduction, the tensile fracture morphology shows that large cleavage surface along with some small-sized dimples was very vague; in fact, it was almost invisible (Fig. 10(c)), which reflected the cleavage fracture characteristics. However, only a small cleavage

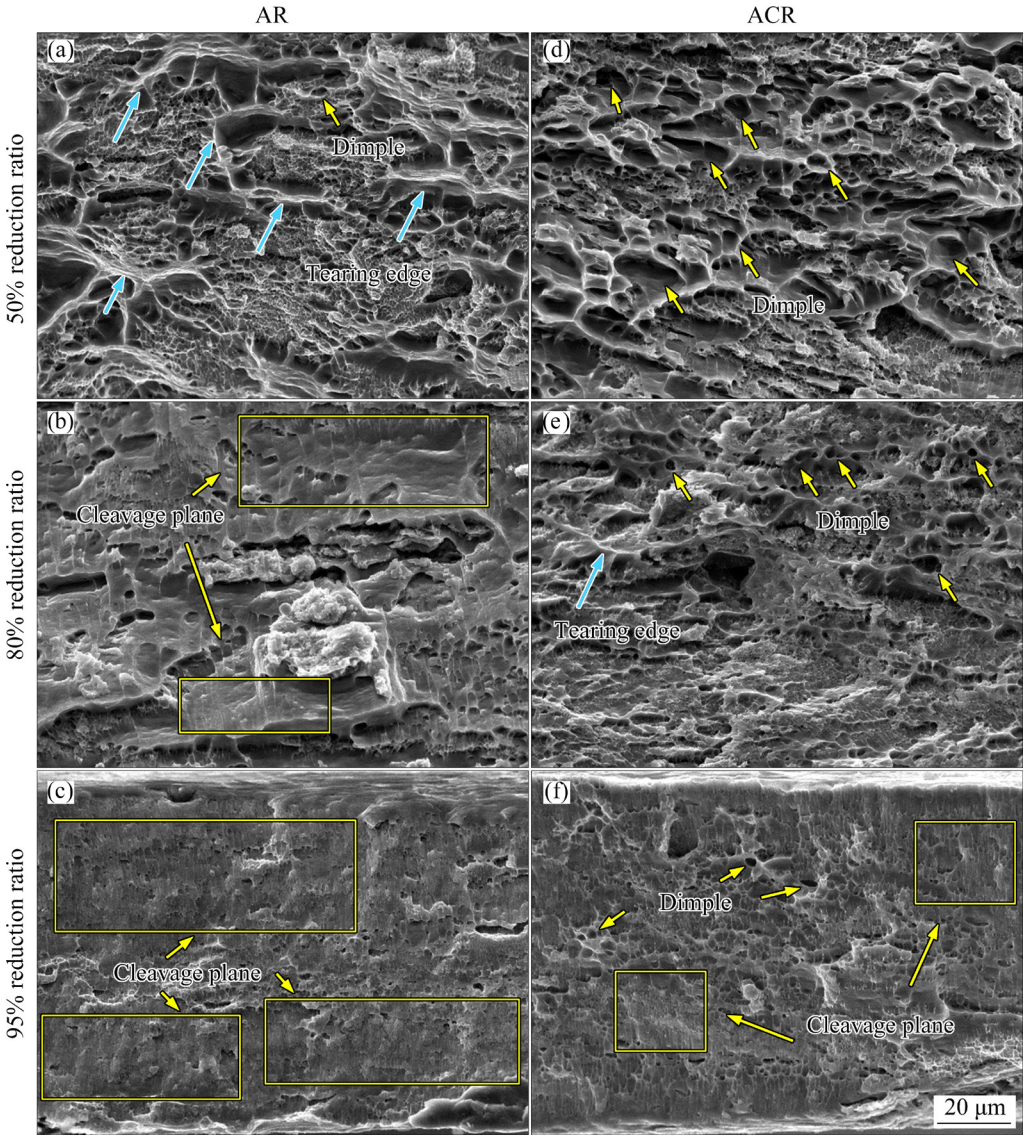

Fig. 10 Fracture morphologies of 3 wt.% HEA_p/AMCs at different rolling reduction ratios

surface in the tensile fracture of ACR HEA_p/AMCs, and a certain number of dimples (Fig. 10(f)), confirmed that the ACR AMCs still possessed a certain ductility [28]. The differences in the tensile fracture morphology were reflected in the mechanical properties as well. It was further confirmed that ACR could improve the elongation of HEA_p/AMCs compared to AR (Fig. 9).

4 Discussion

Figures 4−9 suggest that ACR has a positive effect on ameliorating the microstructure and morphology of the HEA_p/AMCs. The AMCs obtained by the ACR come with fewer defects, such as microvoids. In other words, the ACR process can significantly improve the mechanical properties of AMCs.

4.1 Effect of ACR on microstructure of HEA_p/AMC sheets

Compared with the AR HEA_p/AMCs, the mechanical properties of ACR were quite improved, and the change in the micro defects played an important role. As evident from Figs. 4(b) and 5(a), the AR HEA_p/AMCs possessed microvoid and fracture phenomena. The AR process can refine the size of HEA_p reinforcement to a certain extent by introducing shear deformation. However, if the shear deformation becomes too strong, then it makes more difficulty to coordinate the deformation between HEA_p and the aluminum matrix [29]. Therefore, microvoids and other defects might appear around the HEA_p [30]. The HEA_p reinforcement in ACR HEA_p/AMCs, on the other hand, has an improved microstructure without obvious microvoids. This phenomenon is a result of the volume shrinkage effect [31]. The volume shrinkage of the HEA_p/AMCs occurred at 77 K and could be expressed by [27]

$$V_T = V_0 \exp[\alpha(T - T_0)] \quad (5)$$

where α is the coefficient of thermal expansion (CTE), V is the volume, and T is the temperature. The volume shrinkage effect significantly influences the microstructure and mechanical properties of HEA_p/AMCs [31]. When the HEA_p/AMCs are rolled at room temperature, the deformation of HEA_p and matrix will not be coordinated due to the large difference in elastic modulus between the HEA_p and aluminum matrix, and hence defects might occur around the HEA_p. It is worth noting that the volume shrinkage effect of the aluminum matrix is different from that of the HEA_p reinforcement in the cryogenic environment (77 K). The CTE of aluminum alloy is larger, and the volume shrinkage effect becomes more significant [32]. The HEA_p has a low CTE and a weak volume shrinkage effect [33]. The larger the volume shrinkage effect of the aluminum alloy, the more tightly the aluminum will wrap the HEA_p reinforcement. This will strengthen the bonding between the matrix and HEA_p. Due to the volume shrinkage effect in a cryogenic environment, ACR plays a significant role in avoiding such defects caused by the large plastic deformation of HEA_p/AMC sheets [27]. In addition, the ductility of Al and HEA at cryogenic temperatures is higher than that at room temperature [9]. The enhanced ductility will also contribute to reduced defects in ACR HEA_p/AMC sheets, which in turn enhances their elongation during tensile testing.

4.2 Strengthening mechanism of ACR

The mechanical properties of the HEA_p/AMCs were improved obviously after ACR, as presented in Figs. 8 and 9. In addition to the reduced defects, it was reported that mismatch strengthening of CTE [34], fine grain strengthening [35], and Orowan strengthening [36−38] also play important roles in the enhanced mechanical properties of ACR processed HEA_p/AMC sheets.

CTE mismatch strengthening is a special strengthening method observed in composites. The CTE of HEA_p is different from that of the aluminum matrix [32,33], and the temperature of the composites will change from preparation to processing. Therefore, a residual plastic strain will be generated in the composites, causing an increase in dislocation density [39]. In this study, the deformation temperature of ACR was 77 K, while that of AR was 298 K. The temperature difference between them was about 221 K, which led to a higher dislocation density of ACR HEA_p/AMCs.

The finer grains tend to enhance the mechanical properties. In the cryogenic environment, the lattice of the material will also shrink [40]. As the lattice shrinks, the spacing between the atoms in the material decreases. According to the Peirls−Nabarro equation [41],

there is

$$\tau_{P-N}=[2G/(1-\gamma)]\exp[-2\pi a/(1-\gamma)b] \quad (6)$$

where a is the distance between slip planes, γ is Poisson's ratio, and G is the shearing modulus. When the atomic spacing decreases due to lattice shrink, correspondingly, the lattice resistance to slip dislocations (τ_{P-N}) increases [42,43]. In other words, lattice shrinkage will inhibit dislocation slip, and dislocation pinning will improve the strength of the composite material. In addition, the lattice distortion caused by the huge compressive stress during the process at cryogenic temperature will also promote an increase in dislocation density [44]. Thus, during ACR, dynamic recovery is severely inhibited. Then, a large number of dislocations are irretrievable and difficult to cancel or rearrange [45]. Dislocations are constantly entangled and accumulate, resulting in cellular structures, as shown in Fig. 5(d). A large number of dislocation cells are formed due to the high-density dislocation entanglement in the ACR process, and this extremely high dislocation density will generate subgrains [40]. In cryogenic environments, a large amount of stored energy can accumulate in the composites with high-density dislocations, which can refine grains during rolling [19]. In short, ACR can generate high-density dislocations and substructures in HEA_p/AMCs, thus, improving the comprehensive mechanical properties [46]. The grain size of the ACR HEA_p/AMCs was refined to 179 nm, while that of the AR HEA_p/AMCs was 237 nm, as presented in Fig. 6. Grain boundaries can inhibit dislocation movement, so the stress required for plastic deformation of materials increases, which is reflected in the improvement of the mechanical properties of HEA_p/AMCs during the process of tensile fracture.

Orowan strengthening is a mechanism to enhance the mechanical properties of materials by the hindering effect of dislocations while passing through nanoscale particles [47]. In the present study, it could be observed that the HEA_p in the composites was remarkably refined, and more nanoparticles appeared after the ACR process, as shown in Fig. 4(d). Therefore, the Orowan strengthening mechanism still exists in ACR HEA_p/AMCs.

In summary, the grain size of the HEA_p/AMCs is significantly refined after ACR, and the dislocation density is higher than that of AR HEA_p/AMCs. The plastic deformation during ACR reduces the microvoids and other defects. These factors enhance the comprehensive mechanical properties of the ACR HEA_p/AMCs. Figure 11 presents comparisons of the mechanical properties of ACR HEA_p/AMCs with those of pure Al matrix composites enhanced by some other particles in Refs. [48−53]. Such a comparative study reassures that the ACR HEA_p/AMCs obtained in the present study have excellent mechanical properties.

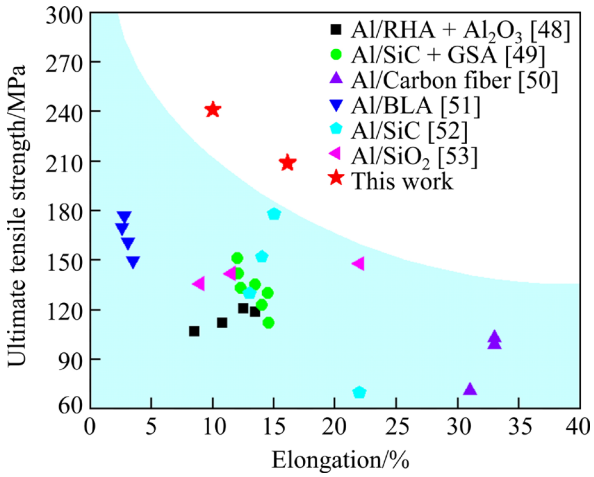

Fig. 11 Comparison of mechanical properties in this study with other reported values [48−53]

5 Conclusions

(1) The ACR process greatly improves the microstructure of the HEA_p/AMCs. The average grain size of 3 wt.% HEA_p/AMCs was 179 and 237 nm, respectively, for ACR and AR processed samples at 95% rolling reduction. The grain size refinement efficiency of ACR 3 wt.% HEA_p/AMCs was enhanced by 24%.

(2) The mechanical properties of the ACR HEA_p/AMCs were improved significantly. The ultimate tensile strength of the ACR 3 wt.% HEA_p/AMC sheets increased from 115 to 253 MPa before rolling, with an approximate increase of 13.5% when compared to that of AR sheets. The HEA_p/AMC sheets exhibited good comprehensive mechanical properties after the ACR process.

(3) In the ACR process, the HEA_p/AMCs suffered a volume shrinkage effect due to the extremely low temperature (77 K), which made the bonding between the HEA_p reinforcement and aluminum matrix stronger.

Acknowledgments

The authors thank the National Key Research and Development Program of China (No. 2019YFB2006500), the High-tech Industry Technology Innovation Leading Plan of Hunan Province, China (No. 2020GK2032), the Innovation Driven Program of Central South University, China (No. 2019CX006), and the Research Fund of the Key Laboratory of High Performance Complex Manufacturing at Central South University, China, for financial support.

References

[1] MISTRY J M, GOHIL P P. Experimental investigations on wear and friction behaviour of $Si3N4_p$ reinforced heat-treated aluminium matrix composites produced using electromagnetic stir casting process [J]. Composites Part B: Engineering, 2019, 161: 190−204.

[2] WANG P, ECKERT J, PRASHANTH K G, WU M W, KABAN I, XI L X, SCUDINO S. A review of particulate-reinforced aluminum matrix composites fabricated by selective laser melting [J]. Transactions of Nonferrous Metals Society of China, 2020, 30: 2001−2034.

[3] ZHANG X, LI S F, PAN D, PAN B, KONDOH K. Microstructure and synergistic-strengthening efficiency of CNTs−SiC_p dual-nano reinforcements in aluminum matrix composites [J]. Composites Part A: Applied Science and Manufacturing, 2018, 105: 87−96.

[4] ZHANG Y, LI X Q, GU H, LI R Q, CHEN P H, KONG C, YU H L. Insight of high-entropy alloy particles-reinforced 2219 Al matrix composites via the ultrasonic casting technology [J]. Materials Characterization, 2021, 182: 111548.

[5] GUPTA R, T NANDA, PANDEY O P. Comparison of wear behaviour of LM13 Al−Si alloy based composites reinforced with synthetic (B_4C) and natural (ilmenite) ceramic particles [J]. Transactions of Nonferrous Metals Society of China, 2021, 31: 3613−3625.

[6] DEY D, BHOWMIK A, BISWAS A. Influence of TiB_2 addition on friction and wear behaviour of Al2024−TiB_2 ex-situ composites [J]. Transactions of Nonferrous Metals Society of China, 2021, 31: 1249−1261.

[7] TOOZANDEHJANI M, OSTOVAN F, JAMALUDIN K R, AMRIN A, MATORI K A, SHAFIEI E. Process−microstructure−properties relationship in Al−CNTs−Al_2O_3 nanocomposites manufactured by hybrid powder metallurgy and microwave sintering process [J]. Transactions of Nonferrous Metals Society of China, 2020, 30: 2339−2354.

[8] MONIKANDAN V V, RAJENDRAKUMAR P K, JOSEPH M A. High temperature tribological behaviors of aluminum matrix composites reinforced with solid lubricant particles [J]. Transactions of Nonferrous Metals Society of China, 2020, 30: 1195−1210.

[9] GLUDOVATZ B, HOHENWARTER A, CATOOR D, CHANG E H, GEORGE E P, RITCHIE R O. A fracture-resistant high-entropy alloy for cryogenic applications [J]. Science, 2014, 345: 1153−1158.

[10] LI J C, LI Y L, WANG F F, MENG X C, WAN L, DONG Z B, HUANG Y X. Friction stir processing of high-entropy alloy reinforced aluminum matrix composites for mechanical properties enhancement [J]. Materials Science and Engineering A, 2020, 792: 139755.

[11] YUAN Z W, TIAN W B, LI F G, FU Q Q, WANG X G, QIAN W F, AN W C. Effect of heat treatment on the interface of high-entropy alloy particles reinforced aluminum matrix composites [J]. Journal of Alloys and Compounds, 2020, 822: 153658.

[12] LIU Y Z, CHEN J, LI Z, WANG X H, FAN X H, LIU J N. Formation of transition layer and its effect on mechanical properties of AlCoCrFeNi high-entropy alloy/Al composites [J]. Journal of Alloys and Compounds, 2019, 780: 558−564.

[13] LUO K G, XIONG H Q, ZHANG Y, GU H, LI Z D, KONG C, YU H L. AA1050 metal matrix composites reinforced by high-entropy alloy particles via stir casting and subsequent rolling [J]. Journal of Alloys and Compounds, 2022, 893: 162370.

[14] LI G R, WEN H R, WANG H M, REN W X, YAN Y W, CHEN J J, WANG C W, ZHAO Y T. Microstructural characteristics and mechanical behavior of microwave-assisted sintered ferromagnetic $FeCoNi_{1.5}CrCu$ HEA_p/Al matrix composites [J]. Journal of Alloys and Compounds, 2021, 861: 158439.

[15] LI Z D, ZHANG Y, XIONG H Q, KONG C, YU H L. Fabrication of particle-reinforced aluminum alloy composite: Role of casting and rolling [J]. Materials and Manufacturing Processes, 2022, 37: 90−98.

[16] ZANCHETTA B D, da SILVA V K, SORDI V L, RUBERT J B, KLIAUGA A M. Effect of asymmetric rolling under high friction coefficient on recrystallization texture and plastic anisotropy of AA1050 alloy [J]. Transactions of Nonferrous Metals Society of China, 2019, 29: 2262−2272.

[17] TÓTH L S, BEAUSIR B, ORLOV D, LAPOVOK R, HALDAR A. Analysis of texture and *R* value variations in asymmetric rolling of IF steel [J]. Journal of Materials Processing Technology, 2012, 212: 509−515.

[18] LI C, XIONG H Q, BHATTA L, WANG L, ZHANG Z Y, WANG H, KONG C, YU H L. Microstructure evolution and mechanical properties of Al−3.6Cu−1Li alloy via cryorolling and aging [J]. Transactions of Nonferrous Metals Society of China, 2020, 30: 2904−2914.

[19] DU Q L, LI C, CUI X H, KONG C, YU H L. Fabrication of ultrafine-grained AA1060 sheets via accumulative roll bonding with subsequent cryorolling [J]. Transactions of Nonferrous Metals Society of China, 2021, 31: 3370−3379.

[20] YU H L, TIEU A K, LU C, LIU X H, GODBOLE A, KONG C. Mechanical properties of Al−Mg−Si alloy sheets produced using asymmetric cryorolling and ageing treatment [J]. Materials Science and Engineering A, 2013, 568: 212−218.

[21] ZHANG Z Y, WU Y Z, BHATTA L, LI C, GAN B, KONG C, WANG Y, YU H L. Mechanical properties and microstructure evolution of a CrCoNi medium entropy alloy subjected to asymmetric cryorolling and subsequent

annealing [J]. Materials Today Communications, 2021, 26: 101776.

[22] KIM J K, KIM J H Z, PARK H, KIM J S, YANG G H, KIM R, SONG T, SUH D W, KIM J. Temperature-dependent universal dislocation structures and transition of plasticity enhancing mechanisms of the Fe40Mn40Co10Cr10 high entropy alloy [J]. International Journal of Plasticity, 2022, 148: 103148.

[23] AHL S R, SIMONS H, DETLEFS C, JENSEN D J, POULSEN H F. Subgrain dynamics during recovery of partly recrystallized aluminum [J]. Acta Materialia, 2020, 185: 142−148.

[24] CHENG W J, LIU W, FAN X B, YUAN S J. Cooperative enhancements in ductility and strain hardening of a solution-treated Al–Cu–Mn alloy at cryogenic temperatures [J]. Materials Science and Engineering A, 2020, 790: 139707.

[25] WANG L, KONG C, YU H L. Mechanical property enhancement and microstructure evolution of an Al−Cu−Li alloy via rolling at different temperatures [J]. Journal of Alloys and Compounds, 2022, 900: 163442.

[26] SHE X W, JIANG X Q, ZHANG R H, WANG P Q, TANG B B, DU W C. Study on microstructure and fracture characteristics of 5083 aluminum alloy thick plate [J]. Journal of Alloys and Compounds, 2020, 825: 153960.

[27] LI J, ZHOU J Z, XU S Q, SHENG J, HUANG S, SUN Y H, SUN Q, BOATENG E A. Effects of cryogenic treatment on mechanical properties and micro-structures of IN718 super-alloy [J]. Materials Science and Engineering A, 2017, 707: 612−619.

[28] KARAMOUZ M, AZARBARMAS M, EMAMY M, ALIPOUR M. Microstructure, hardness and tensile properties of A380 aluminum alloy with and without Li additions [J]. Materials Science and Engineering A, 2013, 582: 409−414.

[29] YAO S J, FENG L, YANG D L, HAN D X, LIU Y, LI Q Q, GUO J H, CHAO B J. A potential hot stamping process for microstructure optimization of 22MnB5 steels characterized by asymmetric pre-rolling and one- or two-step pre-heating [J]. Journal of Materials Processing Technology, 2018, 254: 100−107.

[30] KAZEMI-NAVAEE A, JAMAATI R, AVAL H J. Asymmetric cold rolling of AA7075 alloy: The evolution of microstructure, crystallographic texture, and mechanical properties [J]. Materials Science and Engineering A, 2021, 824: 141801.

[31] GAO Q, JIANG X S, SUN H L, ZHANG Y L, FANG Y J, MO D F, LI X. Performance and microstructure of 4J36/Ni/Cu/V/TC4 welded joints subjected to cryogenic treatment [J]. Materials Letters, 2022, 310: 131504.

[32] GUPTA R, CHAUDHARI G P, DANIEL B S S. Strengthening mechanisms in ultrasonically processed aluminium matrix composite with in-situ Al3Ti by salt addition [J]. Composites Part B: Engineering, 2018, 140: 27−34.

[33] CHOU H P, CHANG Y S, CHEN S K, YEH J W. Microstructure, thermophysical and electrical properties in $Al_xCoCrFeNi$ ($0\leq x\leq 2$) high-entropy alloys [J]. Materials Science and Engineering B, 2009, 163: 184−189.

[34] LI J C, ZHANG X X, GENG L. Effect of heat treatment on interfacial bonding and strengthening efficiency of graphene in GNP/Al composites [J]. Composites Part A: Applied Science and Manufacturing, 2019, 121: 487−498.

[35] GUO B S, SONG M, ZHANG X M, LIU Y Z, CEN X, CHEN B, LI W. Exploiting the synergic strengthening effects of stacking faults in carbon nanotubes reinforced aluminum matrix composites for enhanced mechanical properties [J]. Composites Part B: Engineering, 2021, 211: 108646.

[36] WANG Z, TAN J, SUN B A, SCUDINO S, PRASHANTH K G, ZHANG W W, LI Y Y, ECKERT J. Fabrication and mechanical properties of Al-based metal matrix composites reinforced with Mg65Cu20Zn5Y10 metallic glass particles [J]. Materials Science and Engineering A, 2014, 600: 53−58.

[37] LIU Q B, FAN G L, TAN Z Q, GUO Q, XIONG D B, SU Y S, LI Z Q, ZHANG D. Reinforcement with intragranular dispersion of carbon nanotubes in aluminum matrix composites [J]. Composites Part B: Engineering, 2021, 217: 108915.

[38] ZHANG Q, XIAO B L, WANG W G, MA Z Y. Reactive mechanism and mechanical properties of in situ composites fabricated from an Al−TiO_2 system by friction stir processing [J]. Acta Materialia, 2012, 60: 7090−7103.

[39] ZHU S Z, WANG D, XIAO B L, MA Z Y. Suppressed negative effects of natural aging by pre-aging in SiC_p/6092Al composites [J]. Composites Part B: Engineering, 2021, 212: 108730.

[40] CHE B, LU L W, ZHANG J L, ZHANG J H, MA M, WANG L F, QI F G. Effects of cryogenic treatment on microstructure and mechanical properties of AZ31 magnesium alloy rolled at different paths [J]. Materials Science and Engineering A, 2022, 832: 142475.

[41] LI G R, QIN T, FEI A G, WANG H M, ZHAO Y T, CHEN G, KAI X Z. Performance and microstructure of TC4 titanium alloy subjected to deep cryogenic treatment and magnetic field [J]. Journal of Alloys and Compounds, 2019, 802: 50−69.

[42] LI G R, CHENG J F, WANG H M, LI C Q. The influence of cryogenic-aging circular treatment on the microstructure and properties of aluminum matrix composites [J]. Journal of Alloys and Compounds, 2017, 695: 1930−1945.

[43] WU W W, GUI J Y, ZHU T B, XIE Z P. Role of cryogenic temperature on the strengthening mechanism of SiC_w−Al_2O_3 composites [J]. Ceramics International, 2016, 42: 16332−16335.

[44] LI H G, HUANG Y J, ZHAO W J, CHEN T, SUN J F, WEI D Q, DU Q, ZOU Y C, LU Y Z, ZHU P, LU X, NGAN A H W. Overcoming the strength−ductility trade-off in an additively manufactured CoCrFeMnNi high entropy alloy via deep cryogenic treatment [J]. Additive Manufacturing, 2022, 50: 102546.

[45] PAN Y K, WANG J T, CUI H W, FENG R, GONG B K, ZHAO X C, HOU N, CUI B R, SONG Y R, YANG T. Effect of deep cryogenic treatment on the microstructure and corrosion behavior of the microarc oxidized Mg−2.0Zn−0.5Ca alloy [J]. Journal of Materials Research and Technology, 2020, 9: 3943−3949.

[46] GUO F, DONG H P, HUANG W J, YANG X S, HU L, LI

M D, JIANG L Y. Nanocrystalline structure fabricated by cryogenic temperature rolling of AA 2099 aluminum alloy [J]. Journal of Alloys and Compounds, 2021, 864: 158293.

[47] SABA F, ZHANG F M, LIU S L, LIU T F. Reinforcement size dependence of mechanical properties and strengthening mechanisms in diamond reinforced titanium metal matrix composites [J]. Composites Part B: Engineering. 2019, 167: 7−19.

[48] ALANEME K K, AKINTUNDE I B, OLUBAMBI P A, ADEWALE T M. Fabrication characteristics and mechanical behaviour of rice husk ash – Alumina reinforced Al−Mg−Si alloy matrix hybrid composites [J]. Journal of Materials Research and Technology, 2013, 2: 60−67.

[49] ALANEME K K, BODUNRIN M O, AWE A A. Micro-structure, mechanical and fracture properties of groundnut shell ash and silicon carbide dispersion strengthened aluminium matrix composites [J]. Journal of King Saud University−Engineering Sciences, 2018, 30: 96−103.

[50] ARAB S M, KARIMI S, JAHROMI S A J, JAVADPOUR S, ZEBARJAD S M. Fabrication of novel fiber reinforced aluminum composites by friction stir processing [J]. Materials Science and Engineering A, 2015, 632: 50−57.

[51] KUMAR B P, BIRRU A K. Microstructure and mechanical properties of aluminium metal matrix composites with addition of bamboo leaf ash by stir casting method [J]. Transactions of Nonferrous Metals Society of China, 2017, 27: 2555−2572.

[52] ARAB M S, EL MAHALLAWY N, SHEHATA F, AGWA M A. Refining SiC_p in reinforced Al−SiC composites using equal-channel angular pressing [J]. Materials & Design, 2014, 64: 280−286.

[53] ISSA H K, TAHERIZADEH A, MALEKI A, GHAEI A. Development of an aluminum/amorphous nano-SiO_2 composite using powder metallurgy and hot extrusion processes [J]. Ceramics International, 2017, 43: 14582−14592.

采用深冷异步轧制提高高熵合金颗粒增强铝基复合材料的力学性能

罗开广[1,2]，吴雨泽[1,2]，熊汉青[1,2]，张 昀[1,2]，Charlie KONG[3]，喻海良[1,2,4]

1. 中南大学 极端服役性能精准制造全国重点实验室，长沙 410083；
2. 中南大学 机电工程学院，长沙 410083；
3. Mark Wainwright Analytical Centre, University of New South Wales, Sydney, NSW 2052, Australia;
4. 中南大学 轻合金研究院，长沙 410083

摘 要：为了获得更高性能的铝基复合材料(AMCs)，采用室温异步轧制(AR, 298 K)和深冷异步轧制(ACR, 77 K)制备高熵合金颗粒增强铝基复合材料带材。通过拉伸实验、扫描电子显微镜(SEM)和透射电子显微镜(TEM)对铝基复合材料的力学性能和微观结构进行分析。结果表明，深冷异步轧制比室温异步轧制更能提高复合材料的力学性能。深冷异步轧制含 3%(质量分数)高熵合金颗粒的铝基复合材料的抗拉强度达到 253 MPa，比室温异步轧制复合材料提高 13.5%。与室温异步轧制相比，深冷异步轧制的复合材料具有更少的微孔洞、更细小的晶粒尺寸和更高的位错密度。深冷异步轧制复合材料微缺陷的减少是因为铝基高熵合金颗粒复合材料在深冷环境中具有合适的体积收缩效应。

关键词：铝基复合材料；$Al_{0.5}CoCrFeNi$ 高熵合金颗粒；深冷异步轧制；晶粒尺寸；微观缺陷

(Edited by Bing YANG)